Computer Modeling in Engineering & Sciences
DOI:10.32604/cmes.2020.09118
Article

Analysis of the Quasi-Static Buffeting Responses of Transmission Lines to Moving Downburst

Qigang Sun[1], Jian Wu[1], Dahai Wang[2,*], Yue Xiang[2], Haitao Liu[1] and Xiaobin Sun[3]

[1]Economic and Technology Research Institute of State Grid Shandong Electric Power Company, Jinan, 250000, China
[2]Wuhan University of Technology, Wuhan, 430070, China
[3]State Grid Shandong Electric Power Company, Jinan, 250000, China
*Corresponding Author: Dahai Wang. Email: wangdahai@whut.edu.cn
Received: 13 November 2019; Accepted: 06 February 2020

Abstract: Downburst event is identified as a major cause to failure of transmission lines in non-coastal regions. In this paper, a novel nonlinear analytical frame for quasi-static buffeting responses of hinged and multi-span insulator-line systems are derived based on the theory of cable structure. The closed-form solutions are presented and applied to predict nonlinear response including displacements and other reactions of the system subjected to a moving downburst wind in a case study. Accuracy and efficiency of the derived analytical frame are validated via comparisons with results from finite element method.

Keywords: Downburst; wind; transmission line; buffeting responses; cable; quasi-static

1 Introduction

Transmission line systems are typical wind-sensitive structures. In non-coastal regions, downburst events are identified as major causes to failures of transmission lines. Since transmission line systems are generally hundreds of kilometers long, the downburst events, although occurring locally, are quite common threats to integrity of these wind-sensitive structures [1–3]. Therefore, it is necessary to study strong buffeting responses of the lines-insulator system under downburst.

Unlike synoptic winds, challenges in analyzing the transmission line subjected to downburst arise from nature of such wind, which features highly localized intensity like a thunderstorm. Downburst winds are very different from synoptic atmospheric boundary layer winds in terms of their unique wind speed profile including rapidly varying speed in time domain and strongly correlated wind fluctuations in spatial domain [4–8]. Due to these intriguing complexities, characterizations of downburst-wind effects on structures through numerical simulations and field observations are receiving more and more research attentions [9–19].

Numerical simulations of wind load effects on line-insulator systems generally consist of two parts including wind model and structural response. The wind model is supposed to apply excitations to structures and should help us find a nonstationary velocity field of the wind, which can be generated by empirical mathematical models or computational fluid dynamic (CFD) models of tornado and microburst.

The following structural response is often treated as a quasi-static process and can be handled by finite element method (FEM) analysis. Within such framework, many numerical studies have been conducted to examine effects of downburst parameters on wind-induced vibrational responses of lines. The parameters involve inject scale, intensity and moving path in time domain [20–26]. Aboshosha et al. [27,28] Also, a semi-closed form solution to analyze displacement and reactions of line-insulator systems has been developed.

Experimental investigations to study the downburst effect on multi-span transmission line systems are more straightforward with aeroelastic wind tunnel test and are used as benchmarks for numerical simulations. A four-span transmission line system is tested and the time-varying mean responses from numerical models show good agreement with this testing [29,30].

Numerical simulation and wind tunnel testing both reveal that the dynamic responses of transmission line systems depend on background component of downburst, whereas the resonant component seems negligible, mainly due to aerodynamic damping of the lines. The maximum peak transverse reactions transmitted from lines to support tower are dominated by the mean component and background component. Accordingly, the quasi-static treatment is sufficient in assessing the effect of turbulence of non-synoptic wind. Similar results are also found in behaviors of lines under strong synoptic wind loads [31–33].

In view of above findings, we claim that quasi-static analysis is a proper approach to assess dynamic responses of transmission line systems subjected to downburst loading. We note that the above downburst studies focus on numerical simulations or wind-tunnel testing, while theoretical methods are lacking. Irvine derived a closed-form solution for behaviors of elastic catenary under in-plan distributed and concentrated static loads. Based on these, Wang et al. [34,35] gave a closed-form solution in time and frequency domain to long-span line with joint supports under nonstationary and stationary wind. This solution finds nonlinear static responses to uniform and arbitrary distribution of mean wind load, as well as fluctuation responses to strong non-synoptic or synoptic wind. This solution neglects flexibility of insulators which connects multi-span lines for simplification, which could make an underestimation of longitudinal tension. Consequently, to provide a more accurate prediction of structural responses, we develop a more comprehensive closed-form solution with considerations involving behaviors of the insulators.

In this paper, based on theoretical analysis of hinged cable structures, wind-induced vibrations of insulators and their effects on multi-span transmission lines are investigated. A non-linear analytical framework for quasi-static responses of multi-span transmission-line system subjected to moving downburst is established step by step. We start with single and double-span hinged transmission line and extend the solution to double-span insulator-line system as well as multi-span insulator transmission line system. Results from a case study employing the proposed analytical framework and non-linear FEM are compared for validation.

2 The Analytical Framework of Wind-Induced Quasi-Static Response of Lines under Downburst

2.1 Single-Span Hinged Transmission Line

A horizontal transmission line hinged on both supports at a same level is considered. The structure is modeled as a flat-sag suspended cable with a length of L and a sag-to-span ratio of 1/30. Initial configuration of the line under its uniform gravity mg and a horizontal tension H_0 is denoted as $y_0(x)$, which is in the form of a quadratic function with an initial sag d:

$$y_0(x) = \frac{mg}{2H_0}x(L-x) \tag{1}$$

$$d_0 = \frac{mgL^2}{8H_0} \tag{2}$$

The mean wind speed perpendicular to the line is the most unfavorable wind direction. The mean drag force per unit length of the line is given by:

$$f_D(x,t) = \frac{1}{2}\rho \overline{V}(x,t)^2 D C_D \tag{3}$$

where ρ is air density, $\bar{V}$ is mean time-varying wind speed, C_D is static drag coefficient and D is cross-section diameter of the line. Under static wind load, the line profile $y_0(x)$ changes to a new static equilibrium state $y(x)$ with along wind (horizontal) and crosswind (vertical) static displacements $w(x)$ and $v(x)$ respectively, as shown in Fig. 1. The longitudinal tension and the sag under mean wind load are denoted as H and d. The nonlinear equations of motion of the system under both static wind load and weight are expressed by [36]:

$$H(t)\frac{\mathrm{d}^2(y_0 + v(x,t))}{\mathrm{d}x^2} = -mg \tag{4}$$

$$H(t)\frac{\mathrm{d}^2 w(x,t)}{\mathrm{d}x^2} = -f_D(x,t) \tag{5}$$

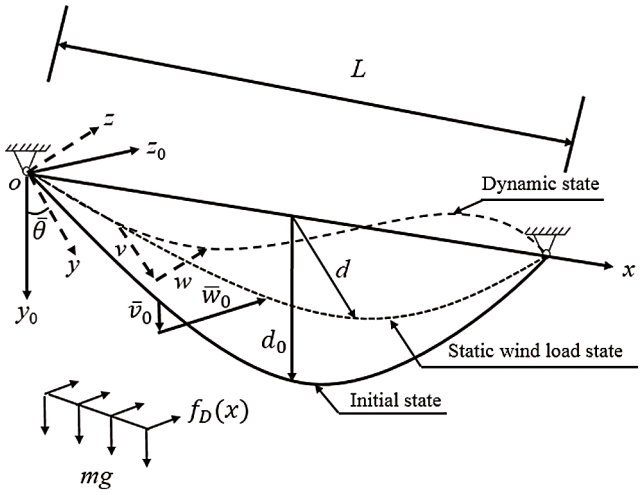

Figure 1: Cable profiles under gravity and wind load

The compatibility condition equation of the line leads to:

$$\frac{(H(t)-H_0)L_e}{EA} = \int_0^L \left(\frac{\mathrm{d}u(x,t)}{\mathrm{d}x} + \frac{\mathrm{d}y_0}{\mathrm{d}x}\frac{\mathrm{d}v(x,t)}{\mathrm{d}x} + \frac{1}{2}\left(\frac{\mathrm{d}v(x,t)}{\mathrm{d}x}\right)^2 + \frac{1}{2}\left(\frac{\mathrm{d}w(x,t)}{\mathrm{d}x}\right)^2\right)\mathrm{d}x \tag{6}$$

where $\bar{u}$ is the static displacement along span-wise direction, E is Young's modulus, A is the cross-section area of the cable, L_e is a virtual length of the cable defined by

$$L_e = \int_0^L \left(1 + \frac{1}{2}\left(\frac{\mathrm{d}y_0}{\mathrm{d}x}\right)^2\right)^{3/2}\mathrm{d}x \approx L \tag{7}$$

The solutions of Eqs. (5) and (6) can be obtained readily by direct integrations considering the boundary conditions:

$$v(x,t) = \frac{(H_0 - H(t))}{H(t)} \frac{mg}{2H_0} x(L-x) \tag{8}$$

$$w(x,t) = \frac{1}{H(t)} \left(\frac{x}{L} \int_0^L \int_0^x (f_D(x,t)\mathrm{d}x_1)\mathrm{d}x_2 - \int_0^x \int_0^x (f_D(x,t)\mathrm{d}x_1)\mathrm{d}x_2 \right) \tag{9}$$

where the boundary conditions for the hinged lines, are $u(0,t) = u(L,t) = v(0,t) = v(L,t) = w(0,t) = w(L,t)$. Substituting Eqs. (8) and (9) to Eq. (6) leads to a simplified compatibility condition Eq. (10) in the form of standard cubic equation $H(t)$. The detailed derivation of Eq. (10) is given in Appendix A.

$$H^3(t) + \left(-H_0 + \frac{EAL^2m^2g^2}{24H_0^2} \right) H^2(t) - \frac{EAL^2q^2(t)}{24} = 0 \tag{10}$$

The time-varying quasi-static tension $H(t)$ at each moment can be obtained by solving Eq. (10). According to force balance equation of the whole transmission line system, the longitudinal reaction T_x, the vertical reaction T_y and the lateral reaction T_z of the transmission line to the support are determined.

$$\begin{cases} T_x(t) = H(t) \\ T_y(t) = -mgL \\ T_z(t) = \int_0^L f_D(x,t)\mu_{T_Z}(x,t)dx \end{cases} \tag{11}$$

where $\mu_{T_Z}(x,t) = 1 - x/L$ is the influence function of T_z (t). It is noted that the T_z (t) as well as T_y (t) are independent of the nonlinear wind-induced yaw status while the T_x (t) relies on the yaw status.

2.2 Double-Span Hinged Lines System

Configurations of double-span hinged lines are shown in Fig. 2, in which 1, 2 and 3 mark three hinged supports. Within a similar analytical framework for each span line, the longitudinal reaction T_{x1}, T_{x2}, vertical reaction T_{y1}, T_{y2}, as well as lateral reaction T_{z1}, T_{z2} are obtained. By superposition, the forces T_x, T_y and T_z of the middle support of the double-span lines are obtained:

$$\begin{cases} T_x(t) = H_2(t) - H_1(t) \\ T_y(t) = -mgL \\ T_z(t) = \int_{-L}^L f_D(x,t)\mu_{T_Z}(x,t)dx \end{cases} \tag{12}$$

where $\mu_{T_Z}(x,t)$ is an influence function of T_z (t).

$$\mu_{T_Z}(x,t) = \begin{cases} 1 + x/L(-L \le x < 0) \\ 1 - x/L(0 \le x \le L) \end{cases} \tag{13}$$

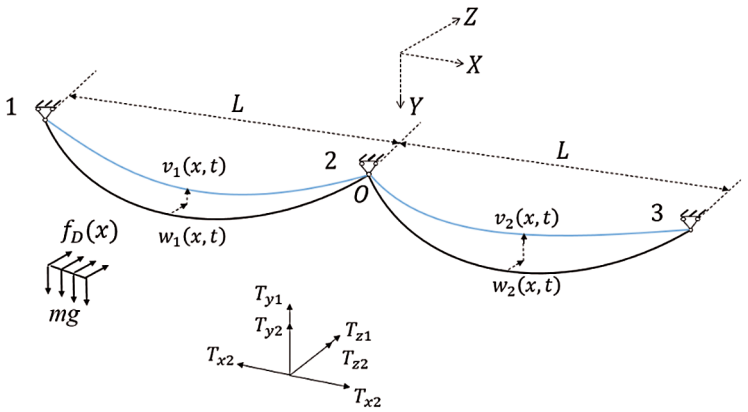

Figure 2: Double-span hinged lines under wind load

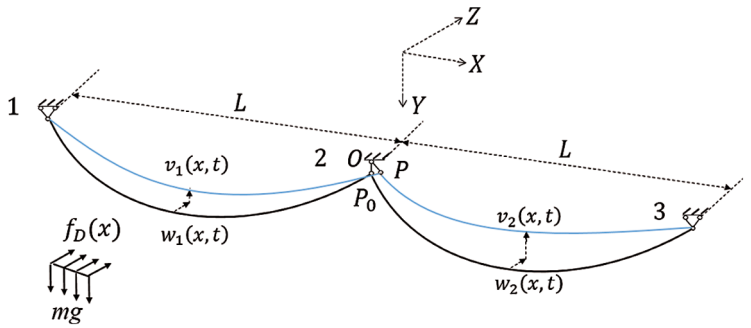

Figure 3: Double-span insulator-line system under wind load

2.3 Double-Span Insulator-Line System

Configurations of double-span insulator-line system are shown in Fig. 3. The calculation of wind-induced vibration of double-span suspended insulator-line under downburst is an extension of the previous discussion of hinged support with considerations of displacements of insulator in three directions. Hence, the deformation compatibility equation of hinged transmission line system should be modified to satisfy both force balance and geometric displacement of insulators.

Supposing the length of the insulator is l, the coordinate system is established with O as the origin, as shown in Fig. 4. When there is no wind load, the insulator is a line object described by OP_0. After wind load is applied, the double-span lines are subjected to a non-axisymmetric distribution of wind loads, the lower end of the insulator moves from P_0 to P under unbalanced tensions T_x, T_y and T_z. Then, the displacements of lower end of insulators OP_x, OP_y and OP_z are u_x, u_y and u_z respectively, the projected lengths of OP_x, OP_y and OP_z on the coordinate axis become l_x, l_y and l_z respectively, as shown in Fig. 4.

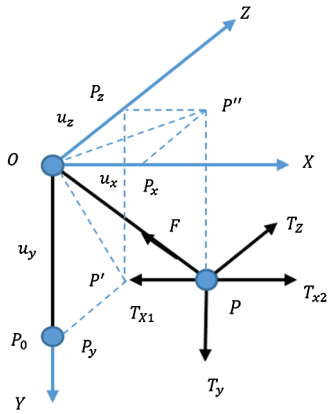

Figure 4: Schematic diagram of stress analysis for lower end of insulator

According to force balance and triangular similarity, it can be found that:

$$l_x^2 + l_y^2 + l_z^2 = l^2 \tag{14}$$

$$T_x : T_y : T_z = l_x : l_y : l_z \tag{15}$$

The relationship between projected lengths and displacements of the lower end of the insulators are:

$$l_x = u_x, l_z = u_z, l_y = l - u_y \tag{16}$$

Eq. (20) can be represented as:

$$\frac{T_x}{T_z}=\frac{u_x}{u_z},\frac{T_x}{T_y}=\frac{u_x}{l_y} \tag{17}$$

The relationships between lateral displacement u_z and longitudinal displacement u_x and between vertical displacement u_y and longitudinal displacement u_x can be obtained by conversions (Eq. (18)).

$$u_z=u_x\frac{T_z}{T_x},u_y=l-u_x\frac{T_y}{T_x} \tag{18}$$

Thus, Eq. (17) can be represented as:

$$\frac{T_x}{\sqrt{T_y^2+T_z^2}}=\frac{u_x}{\sqrt{u_y^2+u_z^2}}=\frac{u_x}{\sqrt{l^2-u_x^2}} \tag{19}$$

Let H_1 be the horizontal tension of the first span transmission line and T_{x1} be the longitudinal reaction between the first span transmission line and the lower end of insulator. Because the displacement u_z at the lower end of insulator in Z direction is very small compared to the span of the entire transmission line, there will be:

$$T_{x1}=H_1\times\frac{L}{\sqrt{u_z^2+L^2}}\approx H_1 \tag{20}$$

Similarly, $T_{x2}\approx H_2$ can be obtained. According to Eqs. (19) and (20), the longitudinal reaction of lines on insulators is:

$$T_x=H_2-H_1=\frac{u_x\sqrt{T_y^2+T_z^2}}{\sqrt{l^2-u_x^2}} \tag{21}$$

Substituting Eq. (19) to Eq. (18) leads to:

$$u_z=\sqrt{\frac{l^2-u_x^2}{1+T_y^2/T_z^2}},u_y=l-\sqrt{\frac{l^2-u_x^2}{1+T_z^2/T_y^2}} \tag{22}$$

The lateral reaction T_z of transmission line on insulator can be calculated from Eq. (12). When the gravity of insulator is small, the vertical reaction T_y of transmission line on insulator can be approximated by gravity G:

$$T_y=-G=-mgL \tag{23}$$

Considering the offset of insulator, there is a longitudinal displacement u_x at the right end of the first span transmission line. The standard form of the compatibility condition of transmission line is simplified by Eq. (10).

$$H_1^3(t)+\left(-H_0-\frac{EAu_x}{L}+\frac{EAL^2m^2g^2}{24H_0^2}\right)H_1^2(t)-\frac{EAL^2q_1^2(t)}{24}=0 \tag{24}$$

where q_1(t) has a same definition in Eq. (10). Similarly, the standard form of one-variable cubic equation for the compatibility condition of the second-span transmission line can be obtained:

$$H_2^3(t)+\left(-H_0-\frac{EAu_x}{L}+\frac{EAL^2m^2g^2}{24H_0^2}\right)H_2^2(t)-\frac{EAL^2q_2^2(t)}{24}=0 \tag{25}$$

where q_2(t) has a same definition in Eq. (10). According to Eq. (25), a third relationship of H_1, H_2 and u_x can be obtained:

$$(H_2(t) - H_1(t))^2 \left(l^2 - u_x^2(t)\right) = u_x^2(t)\left(T_y^2(t) + G^2\right) \tag{26}$$

After solving Eqs. (24)–(26), T_x, u_z and u_y are obtained according to Eqs. (21) and (22). By solving the non-linear equations, the displacements of the lower end of the insulator can be obtained, and then the horizontal tension of two spans can be obtained.

2.4 Multi-Span Insulator-Line System

The deformation of a multi-span insulator-line system under downburst wind is shown in Fig. 5.

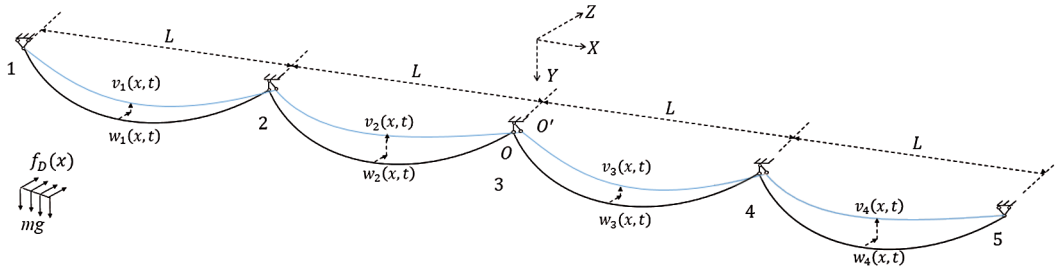

Figure 5: Multiple-spanned line-insulator system under wind load

Considering the compatibility between the deformation of line and insulators, similar to those of the double-span insulator-line system, *i.e.*, Eqs. (24) and (25), the nonlinear tension H_i (*t*) of the *i*th span of *n*-multi-span insulator-line system can be determined by formula below.

$$H_i^3(t) + \left(-H_0 - \frac{EA\left(u_{xi} - u_{x(i-1)}\right)}{L} + \frac{EAm^2g^2L^2}{24H_0^2}\right)H_i^2(t) - \frac{EAq_i^2(t)L^2}{24} = 0 \tag{27}$$

where $i = 1, 2, \ldots, n$ is the number of the span; $u_{x0} = u_{xn} = 0$, $u_{x(i-1)}$ and u_{xi} are displacements of left and right insulators of the *i*-span line respectively. Similar to Eq. (26), the equilibrium of three dimensions forces of the system can be expressed as:

$$(H_{i+1}(t) - H_i(t))^2 \left(l^2 - {u_{xi}}^2(t)\right) - {u_{xi}}^2(t)\left(G^2 + {T_{yi}(t)}^2\right) = 0 \tag{28}$$

where G and $T_{yi}(t)$ are obtainable from Eqs. (12) and (23).

Above analysis for the *n*-multi-span insulator-line system involve $2n - 1$ nonlinear equations in total, which includes n equations in the form of Eq. (27) and $n - 1$ equations in the form of Eq. (28), corresponding to a total of $2n - 1$ unknown variables including n unknowns from H_i and $n - 1$ unknowns from u_{xi}. An iteration scheme is applied to solve the equation set following the algorithm described in Appendix B. Once all H_i and u_{xi} are obtained, the longitudinal reaction T_{xi} on the supports, as well as the vertical displacement u_{yi} and the lateral displacement u_{zi} of the insulator can be obtained by Eqs. (21) and (22).

3 Case Analysis

3.1 Mathematical Model for Downburst

The static average downburst is generated by a mathematical model proposed by Holmes [1] and Wood [10], which is later modified by Li [18]. Due to the dominance of horizontal component of mean velocity, the vertical velocity components are neglected in this paper, as well as some existing studies on downburst, for a

reasonable simplification [3]. The influence of downburst parameters on wind field is comprehensively considered in the model from Li. Accordingly, the wind speed at any point in the wind field can be expressed as follows:

$$u_r = u_m \times u_{m,vs}(z) \times u_{RS}(r) \tag{29}$$

where u_r is horizontal wind speed, u_m is maximum horizontal wind speed (45 m/s in this study), $u_{m,vs}$ (z) is vertical wind profile shape function of the maximum horizontal wind speed, u_{RS} (r) is radial wind profile shape function. The vertical wind profile shape function $u_{m,vs}$ (z) and the radial wind profile shape function u_{RS} (r) of the Li model are expressed as:

$$u_{m,vs}(z) = \left(\frac{z}{z_{um}}\right)^{\gamma} e^{\gamma(1-z/z_{um})} \tag{30}$$

$$u_{RS}(r) = \begin{cases} r/r_m & (r \geq r_m) \\ \exp\left\{-[(r-r_m)/R_c]^{\beta}\right\} & (r \geq r_m) \end{cases} \tag{31}$$

where $\gamma = 0.159$, $z_{um} = 0.0393D_j$, $R_c = 0.599r_m$, and $\beta = 1.287$. Considering the continuous variation of the radial distance r_m corresponding to the maximum horizontal wind speed at different altitudes Z in downburst wind field, r_m is expressed as a function of altitude.

$$r_m(z) = \left[\eta - \frac{z}{r_{mm}} \exp\left(\frac{1-(z/r_{mm})^{2\chi}}{2\chi}\right)\right] D_j \tag{32}$$

where $\eta = 2.1$, $\chi = -0.0363$, $r_{mm} = 0.0078D_j$, Z is the height, and D_j is the diameter of downburst jet.

3.2 Finite Element Model for Lines

The transmission line is modeled in the finite element software ANSYS. The two ends of the line are connected by hinges, and the middle connection is connected by insulators. The insulators are simulated by MPC184 element and the lines are simulated by LINK10 pulling element.

Vector synthesis method is used to combine the static average wind speed of downburst with the moving background wind speed to generate the time-varying average wind load acting on the lines system. The time histories of fluctuations are simulated by the spectral representation method for the target spectrum, and then are uniformly modulated by the magnitude of the time-varying average wind velocity to the non-stationary fluctuations with the constant turbulence intensity 10%. Both the time step in the closed-form solution and FEM are 0.2 s. After the superposition of the fluctuating wind speed and the time-varying average wind speed, the total downburst wind acting on the moving transmission line system can be obtained.

In the case study, moving background wind velocity is set to 12 m/s, descending jet velocity of downburst is 45 m/s with a diameter D_j = 900 m, and attack angle θ is set to 45°. Four-span insulator-line system are simulated by the finite element method. Each span of line is L = 400 m, the length of insulator is l = 4 m, and sag ratio $f = L/30$, as shown in Fig. 6. The initial distance between the centers of the middle tower and the jet r_0 is 3600 m.

3.3 Comparisons between Analytical Solution and Finite Element Method

3.3.1 Comparison of Wind-induced Vibration Responses of Double-Span Insulators and Double-Span Hinged Lines

The longitudinal reaction T_x and lateral reaction T_z of transmission towers from cases with double-span insulator-line system and double-span hinged lines are compared and shown in Fig. 7.

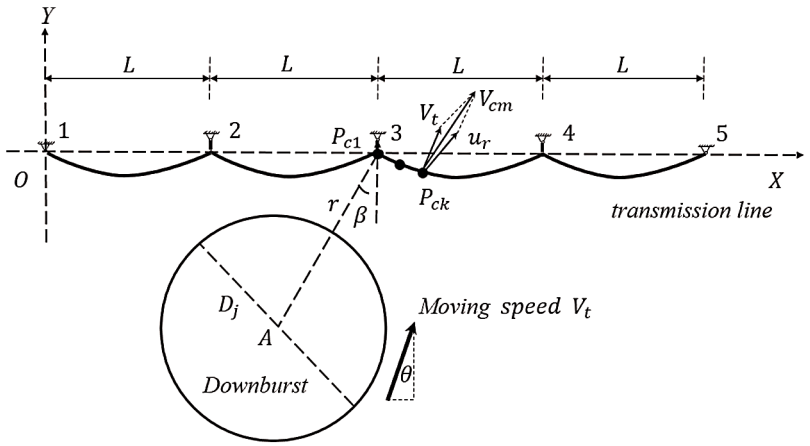

Figure 6: Four-span insulator-line system under downburst

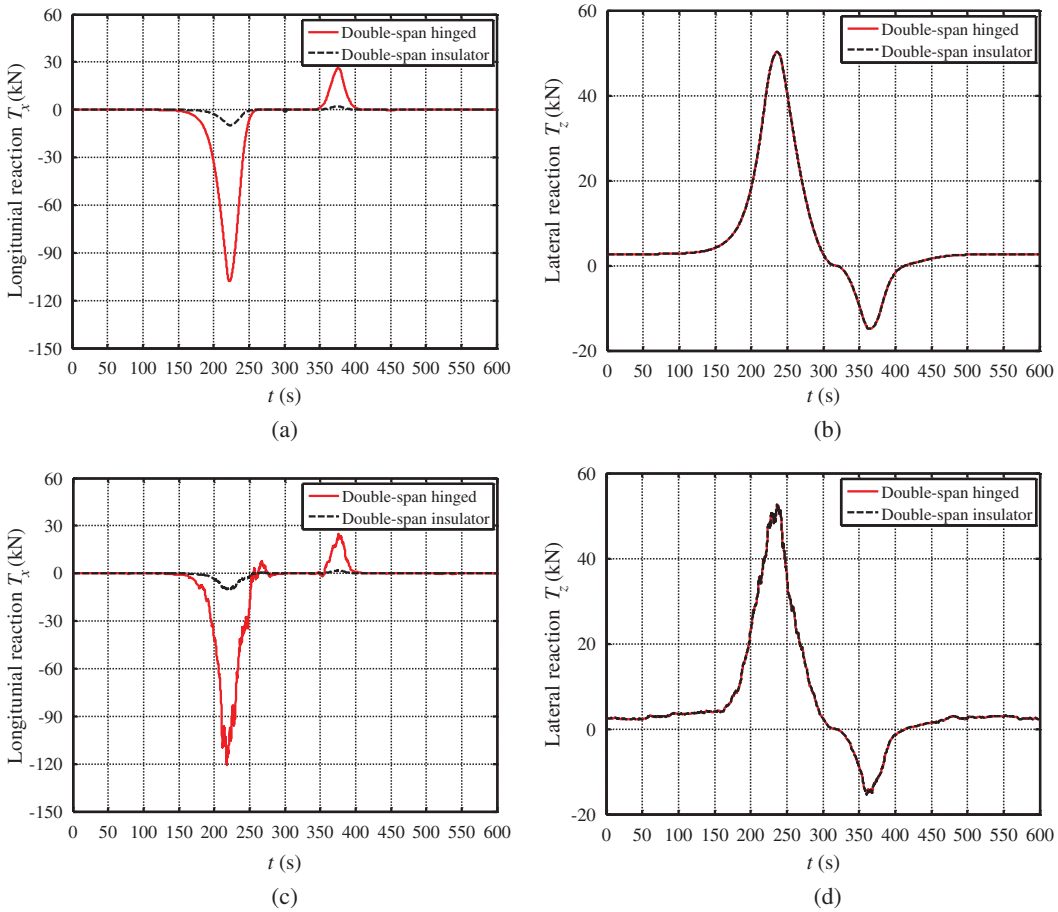

Figure 7: Comparisons of the reaction of two systems to the support under downburst. (a) Longitudinal reaction T_x under mean wind. (b) lateral reaction T_z under mean wind (c) Longitudinal reaction T_x under full wind (d) lateral reaction T_z under full wind

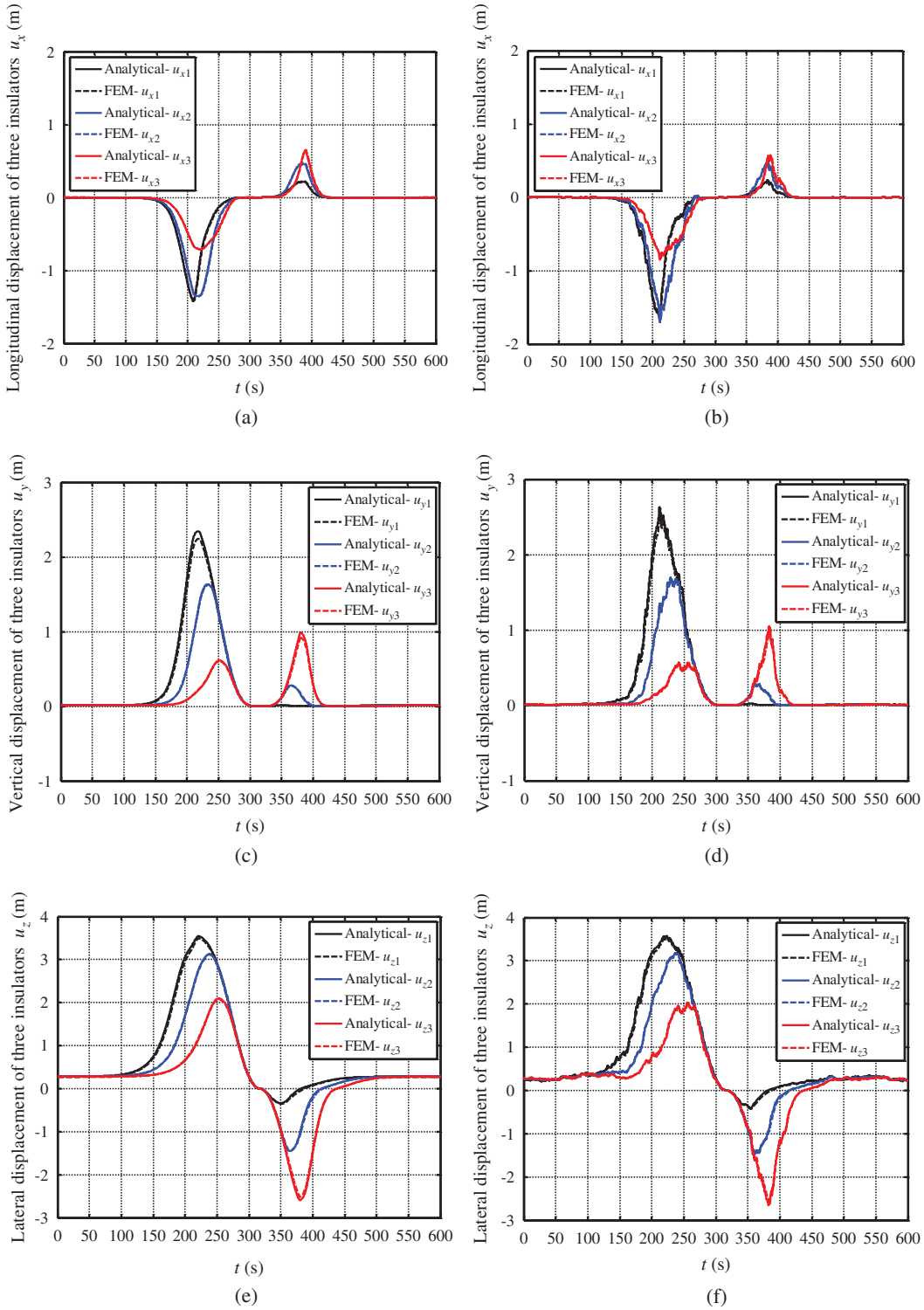

Figure 8: Longitudinal and lateral displacement of four-span insulator-line to Support. (a) Longitudinal displacement u_x under mean wind. (b) Longitudinal displacement u_x under full wind. (c) Vertical displacement u_y under mean wind. (d) Vertical displacement u_y under full wind. (e) lateral displacement u_z under mean wind. (f) lateral displacement u_z under full wind

It is found that the lateral reactions of the middle support under the two systems are similar and are not affected by the connection mode. However, the longitudinal reaction of hinged connection is significantly greater than that of insulator connection, showing that the longitudinal reactions are affected by the connection mode. The reason is that the different wind load distributions will lead to unbalanced longitudinal tension between two spans. When the insulators are connected, the motion of end of the insulators will releases the unbalanced longitudinal reactions and subsequently reduces the longitudinal load on transmission tower.

3.3.2 Four-Span Suspended Insulator Transmission Line System

The responses of the end support reaction and displacement of the four-span insulator-line system using the theoretical frame mentioned in Chapter 2.4 are compared with those of the nonlinear finite element method, as shown in Figs. 8 and 9.

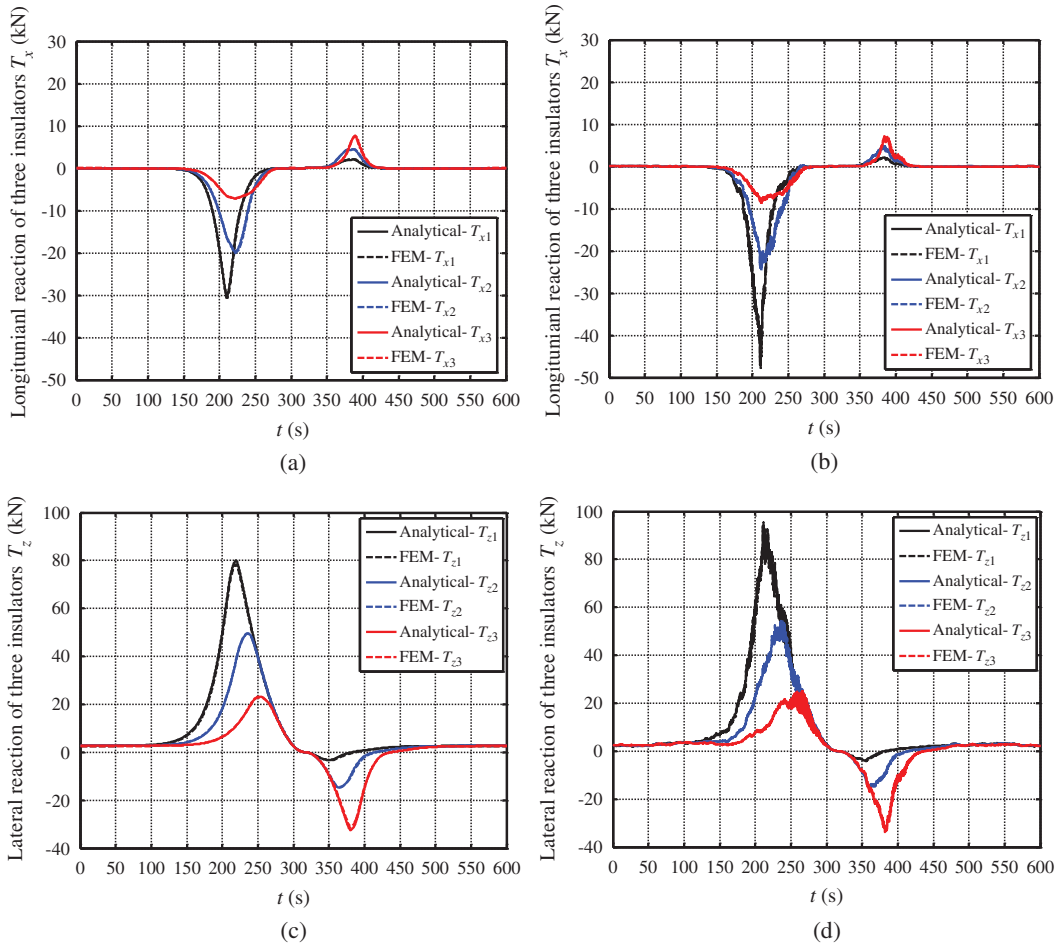

Figure 9: Longitudinal and lateral reaction of four-span insulator-line to Support. (a) Longitudinal reaction T_x under mean wind. (b) Longitudinal reaction T_x under full wind. (c) lateral reaction Tz under mean wind. (d) lateral reaction T_z under full wind

In Fig. 8, it can be found that the time history of displacement response at the three insulator ends are similar with a short delay only. When the downburst approaches the lines gradually (0~300 s), displacements in three directions increase gradually and reaching the peak value. When center of the downburst passes

through the lines (t = 300 s), bottom displacement of insulators in three directions gradually decreases to 0. After the downburst center leaves the lines (300~600 s), displacements gradually reach the maximum in reverse direction, then begin to decrease.

Fig. 9 shows that the time history of reaction forces are similar with the displacement responses. Because (i) the lateral reaction force T_z can be determined directly by the time-independent linear influence function, as given in Eq. (17) and (ii) the fluctuation wind load are relatively smaller than the time-varying mean wind, the differences of T_z under the mean wind and the full wind are insignificant. In terms of T_x, the peak values in mean and full wind are largely different, corresponding to nonlinear characteristics of the system. Among the three supports, the longitudinal reaction T_{x1}, at the 1st insulator in the moving-wind-ward direction, is the largest one, almost half of the lateral reaction T_{z1}. The vertical tension T_y of insulators to towers largely depends on gravity of lines in quasi-static analysis and it remains constant during the downburst process. Therefore, it is not discussed here.

4 Conclusions

This study presents an analysis framework with closed-form formulations for estimating buffeting responses of transmission lines under localized moving downburst wind excitation. The theoretical solutions of the nonlinear quasi-static responses are derived for any arbitrary spatial and temporal distribution of the non-synoptic wind load. The accuracy and validity of the analytical frame are demonstrated by comparisons with a nonlinear finite element method. From the results, 3 concluding remarks can be drawn.

1. The closed-form solution shows good agreement with results of the non-linear finite element method in terms of both the lateral and longitudinal reactions as well as the displacements of lines and insulators. Due to a large amount of nonlinear elements in the FEM model of multi-span insulator-line system, the numerical simulation consumes more computational power than the proposed analytical framework, which behaves more efficiently.
2. During the attack of the moving downburst, the lateral and longitudinal reactions and displacements of insulators will increase firstly with the downburst approaching, then will decrease gradually and even turn to an opposite direction when the downburst passes and leaves the system. Though, peak values always occur during the approaching stage. Different responses between the time-varying-mean and full wind cases show nonlinear features of the system.
3. As longitudinal sway of the insulators would release unbalanced tension found in the case of hinged supports, connection with insulators will significantly reduce the longitudinal reaction of the lines under downburst. Obviously, this effect will lead to a decrease in the longitudinal wind load action, which might be attributed to the destruction of the transmission tower under localized and intensive downburst wind.

Acknowledgement: These supports by Science and Technology Foundation of State Grid Shandong Electric Power Company (Grant No. 52062518000U) and National Natural Science Foundation of China (Grant Nos. 51720105005 and 51478373) are greatly acknowledged.

Funding Statement: This work is supported in part by Science and Technology Foundation of State Grid Shandong Electric Power Company (Grant No. 52062518000U) and National Natural Science Foundation of China (Grant Nos. 51720105005 and 51478373).

Conflicts of Interest: The authors declare that they have no conflicts of interest to report regarding the present study.

References

1. Holmes, J. D., Hangan, H. M., Schroeder, J. L., Letchford, C. W., Orwig, K. D. (2008). A forensic study of the Lubbock-Reese downdraft of 2002. *Wind and Structures, 11(2),* 137–152. DOI 10.12989/was.2008.11.2.137.
2. Shehata, A. Y., El Damatty, A. A. (2008). Failure analysis of a transmission tower during a microburst. *Wind and Structures, 11(3),* 193–208. DOI 10.12989/was.2008.11.3.193.
3. Aboshosha, H., Elawady, A., El Ansary, A., El Damatty, A. (2016). Review on dynamic and quasi-static buffeting response of transmission lines under synoptic and non-synoptic winds. *Engineering Structures, 112,* 23–46. DOI 10.1016/j.engstruct.2016.01.003.
4. Fujita, T. T. (1990). Downbursts: meteorological features and wind field characteristics. *Journal of Wind Engineering and Industrial Aerodynamics, 36,* 75–86. DOI 10.1016/0167-6105(90)90294-M.
5. Milford, R. V., Goliger, A. M. (1997). Tornado risk model for transmission line design. *Journal of Wind Engineering and Industrial Aerodynamics, 72,* 469–478. DOI 10.1016/S0167-6105(97)00262-6.
6. Letchford, C. W., Mans, C., Chay, M. T. (2002). Thunderstorms—their importance in wind engineering (a case for the next generation wind tunnel). *Journal of Wind Engineering and Industrial Aerodynamics, 90(12),* 1415–1433. DOI 10.1016/S0167-6105(02)00262-3.
7. Choi, E. C. (2004). Field measurement and experimental study of wind speed profile during thunderstorms. *Journal of Wind Engineering and Industrial Aerodynamics, 92(3),* 275–290. DOI 10.1016/j.jweia.2003.12.001.
8. Orwig, K. D., Schroeder, J. L. (2007). Near-surface wind characteristics of extreme thunderstorm outflows. *Journal of Wind Engineering and Industrial Aerodynamics, 95(7),* 565–584. DOI 10.1016/j.jweia.2006.12.002.
9. Oliver, S. E., Moriarty, W. W., Holmes, J. D. (2000). A risk model for design of transmission line systems against thunderstorm downburst winds. *Engineering Structures, 22(9),* 1173–1179. DOI 10.1016/S0141-0296(99)00057-7.
10. Wood, G. S., Kwok, K. C., Motteram, N. A., Fletcher, D. F. (2001). Physical and numerical modelling of thunderstorm downbursts. *Journal of Wind Engineering and Industrial Aerodynamics, 89(6),* 535–552. DOI 10.1016/S0167-6105(00)00090-8.
11. Hangan, H., Roberts, D., Xu, Z., Kim, J. (2003). Downburst simulation: experimental and numerical challenges. *Proceedings of the 11th International Conference on Wind Engineering, Lubbock, TX, Electronic Version.*
12. Kareem, A., Butler, K., Kwon, D. (2006). Modeling and simulation of transient wind load effects. *Proceedings of the 4th UJNR Panel on Wind and Seismic Effects Workshop on Wind Engineering, Tsukuba, Tokyo.*
13. Kim, J., Hangan, H. (2007). Numerical simulations of impinging jets with application to downbursts. *Journal of Wind Engineering and Industrial Aerodynamics, 95(4),* 279–298. DOI 10.1016/j.jweia.2006.07.002.
14. Chay, M. T., Wilson, R., Albermani, F. (2008). Gust occurrence in simulated non-stationary winds. *Journal of Wind Engineering and Industrial Aerodynamics, 96(10),* 2161–2172. DOI 10.1016/j.jweia.2008.02.059.
15. Fu, X., Li, H. N., Li, G. (2016). Fragility analysis and estimation of collapse status for transmission tower subjected to wind and rain loads. *Structural Safety, 58,* 1–10. DOI 10.1016/j.strusafe.2015.08.002.
16. Fu, X., Li, H., Li, G., Dong, Z. (2020). Fragility analysis of a transmission tower under combined wind and rain loads. *Journal of Wind Engineering and Industrial Aerodynamics, 199,* 104098. DOI 10.1016/j.jweia.2020.104098.
17. Solari, G., De Gaetano, P., Repetto, M. P. (2015). Thunderstorm response spectrum: fundamentals and case study. *Journal of Wind Engineering and Industrial Aerodynamics, 143,* 62–77. DOI 10.1016/j.jweia.2015.04.009.
18. Li, C., Li, Q. S., Xiao, Y. Q., Ou, J. P. (2012). A revised empirical model and CFD simulations for 3D axisymmetric steady-state flows of downbursts and impinging jets. *Journal of Wind Engineering and Industrial Aerodynamics, 102,* 48–60. DOI 10.1016/j.jweia.2011.12.004.
19. Shao, H. J., Deng, X. (2018). AdaBoosting neural network for short-term wind speed forecasting based on seasonal characteristics analysis and lag space estimation. *Computer Modeling in Engineering & Sciences, 114(3),* 277–293.
20. Savory, E., Parke, G. A., Zeinoddini, M., Toy, N., Disney, P. (2001). Modelling of tornado and microburst-induced wind loading and failure of a lattice transmission tower. *Engineering Structures, 23(4),* 365–375. DOI 10.1016/S0141-0296(00)00045-6.

21. Shehata, A. Y., El Damatty, A. A., Savory, E. (2005). Finite element modeling of transmission line under downburst wind loading. *Finite Elements in Analysis and Design, 42(1),* 71–89. DOI 10.1016/j.finel.2005.05.005.
22. Chay, M. T., Albermani, F. G., Hawes, H. (2006). Wind loads on transmission line structures in simulated downbursts. *First World Congress on Asset Management, Gold Coast, Australia*.
23. Shehata, A. Y., El Damatty, A. A. (2007). Behaviour of guyed transmission line structures under downburst wind loading. *Wind and Structures, 10(3),* 249–268. DOI 10.12989/was.2007.10.3.249.
24. Ren, W. X., Su, C. C., Yan, W. J. (2010). Dynamic modeling and analysis of arch bridges using beam-arch segment assembly. *Computer Modeling in Engineering & Sciences, 70(1),* 67–92.
25. Darwish, M. M., El Damatty, A. A. (2011). Behavior of self-supported transmission line towers under stationary downburst loading. *Wind and Structures, 14(5),* 481–498. DOI 10.12989/was.2011.14.5.481.
26. Hamada, A., El Damatty, A. A. (2011). Behavior of guyed transmission line structures under tornado wind loading. *Computers & Structures, 89(11),* 986–1003. DOI 10.1016/j.compstruc.2011.01.015.
27. Aboshosha, H., El Damatty, A. (2014). Effective technique to analyze transmission lines under high intensity winds. *Wind and Structures, 18(3),* 235–252. DOI 10.12989/was.2014.18.3.235.
28. Aboshosha, H., El Damatty, A. (2015). Dynamic response of transmission line lines under downburst and synoptic winds. *Wind and Structures, 21(2),* 241–272. DOI 10.12989/was.2015.21.2.241.
29. Elawady, A., Aboshosha, H., El Damatty, A., Bitsuamlak, G. (2016). Wind tunnel testing of a multiple span aeroelastic transmission line subjected to downburst wind. *Proceeding of the General Conference of the Canadian Society of Civil Engineering, London, ON, Canada.*
30. Elawady, A., Aboshosha, H., El Damatty, A. (2018). Aero-elastic response of transmission line system subjected to downburst wind: validation of numerical model using experimental data. *Wind and Structures, 27(2),* 71–88.
31. Matheson, M. J., Holmes, J. D. (1981). Simulation of the dynamic response of line in strong winds. *Engineering Structures, 3(2),* 105–110. DOI 10.1016/0141-0296(81)90036-5.
32. Loredo-Souza, A. M., Davenport, A. G. (1998). The effects of high winds on line. *Journal of Wind Engineering and Industrial Aerodynamics, 74,* 987–994. DOI 10.1016/S0167-6105(98)00090-7.
33. Hung, P. V., Yamaguchi, H., Isozaki, M., Gull, J. H. (2014). Large amplitude vibrations of long-span transmission lines with bundled lines in gusty wind. *Journal of Wind Engineering and Industrial Aerodynamics, 126,* 48–59. DOI 10.1016/j.jweia.2014.01.002.
34. Irvine, H. M. (1981). *Cable structures*. Cambridge: MIT Press.
35. Wang, D., Chen, X., Yang, L. (2016). Prediction of wind-induced dynamic response of overhead transmission lines. *8th International Colloquium on Bluff Body Aerodynamics and Applications*. Northeastern University, Boston, MA, USA.
36. Wang, D., Chen, X., Li, J. (2017). Prediction of wind-induced buffeting response of overhead line: comparison of linear and nonlinear analysis approaches. *Journal of Wind Engineering & Industrial Aerodynamics, 167,* 23–40. DOI 10.1016/j.jweia.2017.04.008.

Appendix A. The Simplified Compatibility Condition Equation for the Hinged Lines under Arbitrary Lateral Loading

When the two ends of the lines are hinged, the static displacement at the ends along span-wise direction, i.e., $\bar{u}(x,t)$, is equal to zero and the first item in the right side of Eq. (6) equals zero too. After integrating by parts and considering the static differential equation of the line under the gravity $H\mathrm{d}^2y_0/\mathrm{d}x^2 = -mg$, the second item in the right side of the Eq. (6) can be rewritten as:

$$\int_0^L \frac{dy_0}{dx}\frac{dv(x,t)}{dx}\mathrm{d}x = -\frac{mg}{H_0}\int_0^L v(x,t)\mathrm{d}x \tag{A1}$$

Substituting Eq. (8) into Eq. (A2) leads to:

$$-\frac{mg}{H_0}\int_0^L v(x,t)\mathrm{d}x = \frac{(mg)^2(H_0 - H(t))L^3}{12H_0^2H(t)} \tag{A2}$$

Substituting Eq. (8) into the third item in the right side of Eq. (6) gives:

$$\frac{1}{2}\int_0^L \left(\frac{\mathrm{d}v(x,t)}{dx}\right)^2 \mathrm{d}x = \frac{m^2g^2(H_0 - H(t))^2L^3}{24{H_0}^2H(t)^2} \tag{A3}$$

Substituting Eq. (9) into the forth item in the right side of Eq. (6) gives:

$$\frac{1}{2}\int_0^L \left(\frac{\mathrm{d}w(x,t)}{dx}\right)^2 \mathrm{d}x = \frac{L^3f_*^2(t)}{24H(t)^2} \tag{A4}$$

where $f_*^2(t)$ can be considered as the equivalent uniform load for the arbitrary distribution load $\bar{f}_D(x,t)$ and it is given as:

$$f_*^2(t) = \frac{12}{L^3}\int_0^L \left[\int_0^L f_D(x,t)\left(1 - \frac{x}{L}\right)\mathrm{d}x_1 - \int_0^x f_D(x,t)\mathrm{d}x_1\right]^2 \mathrm{d}x_2 \tag{A5}$$

When $f_D(x,t)$ follows a uniform distribution along span, i.e., $f_D(x,t) = f_D(t)$, we have $f_*(t) = f_D(t)$. Substitution of Eqs. (A2)–(A4) to Eq. (6) leads to the following Eq. (10), which can be used to determine the horizontal tension $H(t)$:

$$H^3(t) + \left(-H_0 + \frac{EAL^2m^2g^2}{24H_0^2}\right)H^2(t) - \frac{EAL^2q^2(t)}{24} = 0 \tag{A6}$$

where the resultant forces is denoted by $q(t)$ and can be expressed by:

$$q(t) = \sqrt{(mg)^2 + f_*^2(t)} \tag{A7}$$

Appendix B. The Flow Chart of the Iteration Scheme Used to Solve the Nonlinear Equations of H_i and u_{xi} in Eqs. (28) and (29)

A quasi-Newton method, Broyden iteration method is employed to solve Eqs. (28) and (29) at time t, formula of the iteration scheme are given below.

$$\boldsymbol{x}^{(k+1)} = \boldsymbol{x}^{(k)} - \boldsymbol{A}^{(k)^{-1}}\boldsymbol{f}\left(\boldsymbol{x}^{(k)}\right) \tag{B1}$$

where $\boldsymbol{x}$ is the unknown variable vector in the Eqs. (28) and (29).

$$\boldsymbol{x} = \left\{\boldsymbol{H_1}, \ldots \boldsymbol{H_n},\ \boldsymbol{u_{x1}}, \ldots \boldsymbol{u_{x(n-1)}}\right\}_{\boldsymbol{2n-1}} \tag{B2}$$

At each time step t, the initial estimation of H_i and u_{xi} can be obtained in previous time step $t - \Delta t$.

$$\boldsymbol{x}_{\boldsymbol{t}}^{(\boldsymbol{0})} = \left\{\boldsymbol{H}_{\boldsymbol{1}_{t-\Delta t}}, \ldots \boldsymbol{H}_{\boldsymbol{i}_{t-\Delta t}},\ \boldsymbol{u_{x1}}_{t-1}, \ldots \boldsymbol{u_{xi}}_{t-\Delta t}\right\} \tag{B3}$$

At time step $t = 0$, assuming the center of the downburst is far away from the transmission lines system, set the initial longitudinal tension of lines and displacements of insulator $H_i = H_0$ and $u_{xi} = 0$. $\boldsymbol{f}$ is a nonlinear equation vector composed of Eqs. (28) and (29).

$$\boldsymbol{f} = \begin{Bmatrix} H_{1t}^3 + \left(-H_0 - \dfrac{EA(u_{x1t} - u_{x0t})}{L} + \dfrac{EAm^2g^2L^2}{24H_0^2}\right)H_{it}^2 - \dfrac{EAq_{it}^2L^2}{24} \\ \vdots \\ H_{nt}^3 + \left(-H_0 - \dfrac{EA\left(u_{xnt} - u_{x(n-1)_t}\right)}{L} + \dfrac{EAm^2g^2L^2}{24H_0^2}\right)H_{it}^2 - \dfrac{EAq_{it}^2L^2}{24} \\ (H_2(t) - H_1(t))^2(l^2 - u_{x1}^2(t)) - u_{x1}^2(t)\left(T_{y1}^2(t) + G^2\right) \\ \vdots \\ (H_n(t) - H_{n-1}(t))^2(l^2 - u_{xn}^2(t)) - u_{xn}^2(t)\left(T_{yn}^2(t) + G^2\right) \end{Bmatrix}_{2n-1} \tag{B4}$$

$\boldsymbol{A}$ is denoted as the iteration matrix. It is given as:

$$\boldsymbol{A}^{(k+1)} = \boldsymbol{A}^{(k)} + \frac{\left(\boldsymbol{q}^{(k)} - \boldsymbol{A}_k\boldsymbol{p}^{k(k)}\right)\left(\boldsymbol{p}^{(k)}\right)^{\mathrm{T}}}{\boldsymbol{p}^{(k)}\left(\boldsymbol{p}^{(k)}\right)^{\mathrm{T}}} \qquad (k > 1) \tag{B5}$$

where $\boldsymbol{p}^{(k)} = \boldsymbol{x}^{(k+1)} - \boldsymbol{x}^{(k)}$, $\boldsymbol{q}^{(k)} = \boldsymbol{f}^{(k+1)} - \boldsymbol{f}^{(k)}$. The initial $\boldsymbol{A_0}$ can be set as the first-order partial derivative of $\boldsymbol{f}$, *i.e.*, $\boldsymbol{A}^{(0)} = \boldsymbol{f}'\left(\boldsymbol{x}^{(0)}\right)$

$$\boldsymbol{A}^{(0)} = \boldsymbol{f}'\left(\boldsymbol{x}^{(0)}\right) = \begin{bmatrix} \dfrac{\partial f_1}{\partial H_1} \cdots \dfrac{\partial f_1}{\partial H_n} \dfrac{\partial f_1}{\partial u_{x1}} \cdots \dfrac{\partial f_1}{\partial u_{x(n-1)}} \\ \vdots \\ \dfrac{\partial f_{2n-1}}{\partial H_1} \cdots \dfrac{\partial f_{2n-1}}{\partial H_n} \dfrac{\partial f_{2n-1}}{\partial u_{x_1}} \cdots \dfrac{\partial f_{2n-1}}{\partial u_{x_{n-1}}} \end{bmatrix}_{(2n-1)\times(2n-1)} \tag{B6}$$

The following flow chart, as shown in Fig. B1, illustrates an iteration at time step t in detail.

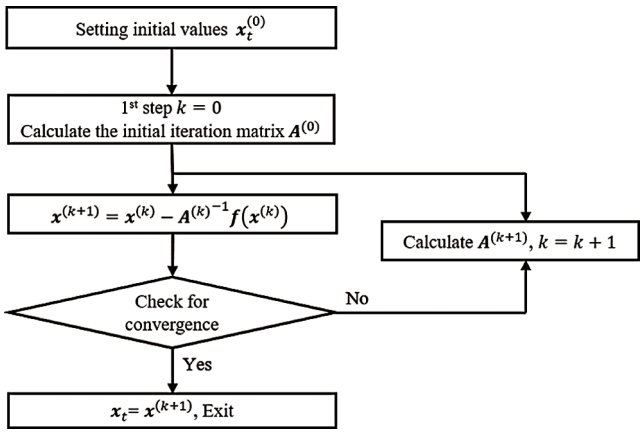

Figure B1: Flowchart of one iteration in the solution to the nonlinear equations